

## REPORT

## LASER PHYSICS

## Widely tunable compact terahertz gas lasers

Paul Chevalier<sup>1</sup>, Arman Armizhan<sup>1</sup>, Fan Wang<sup>2</sup>, Marco Piccardo<sup>1</sup>, Steven G. Johnson<sup>3,4</sup>, Federico Capasso<sup>1,x</sup>, Henry O. Everitt<sup>5,6\*</sup>

The terahertz region of the electromagnetic spectrum has been the least utilized owing to inadequacies of available sources. We introduce a compact, widely frequency-tunable, extremely bright source of terahertz radiation: a gas-phase molecular laser based on rotational population inversions optically pumped by a quantum cascade laser. By identifying the essential parameters that determine the suitability of a molecule for a terahertz laser, almost any rotational transition of almost any molecular gas can be made to lase. Nitrous oxide is used to illustrate the broad tunability over 37 lines spanning 0.251 to 0.955 terahertz, each with kilohertz linewidths. Our analysis shows that laser lines spanning more than 1 terahertz with powers greater than 1 milliwatt are possible from many molecular gases pumped by quantum cascade lasers.

The problem of generating terahertz-frequency radiation (0.3 to 3.0 THz)—in the middle of the electromagnetic spectrum between the microwave region and the infrared (IR) region—has challenged researchers for decades. Not only would wireless communications and radar benefit from operating in the terahertz region, because of appealing characteristics such as high bandwidth, high spatial resolution, compact size, and/or adjustable atmospheric propagation (1), but so would applications requiring stable local oscillators, such as spectroscopy and astronomical observations of the interstellar media. Among the many techniques developed to generate terahertz radiation, the most widely used (2) include harmonic multipliers of tunable microwave sources (3), vacuum electronics (backward-wave oscillators, gyrotrons, and carcinotrons) (4), supercontinua generated by ultrafast lasers and photoconductive switches (5), and difference-frequency mixing of tunable continuous-wave lasers (6–8). Commercial versions of each of these terahertz sources are becoming increasingly available and powerful, but none of them produce much power near 1 THz, and their cost and idiosyncrasies have prevented widespread adoption. Terahertz quantum cascade lasers (9) are compact and can span portions

of the region, but they currently have limited fractional tunability (<25%) and operate below room temperature (10, 11).

Often overlooked is one of the earliest sources of terahertz radiation, optically pumped far-infrared (OPFIR) lasers (12). These gas-phase lasers use a discretely line-tunable carbon dioxide (CO<sub>2</sub>) laser to excite a specific rotational-vibrational (ro-vibrational) transition in a specific molecular gas to create a rotational population inversion within a tunable cavity. These lasers generate appreciable power (up to 100 mW) and exhibit a narrow linewidth ( $\Delta\nu < 10$  kHz), a combination of features that is not available with most other terahertz sources. However, OPFIR lasers are inefficient, large (~1 m), and require an equally large CO<sub>2</sub> laser and high-voltage power supply. Moreover, they are poorly tunable, requiring the laser gas and CO<sub>2</sub> laser line to be changed each time a different frequency is needed. Consequently, OPFIR lasers fell from widespread use when other sources became available.

Here, we introduce an OPFIR laser concept characterized by frequency tunability over the entire range of rotational transitions from the molecular gas gain medium. Broad terahertz tunability is made possible by using a continuously tunable mid-IR pump source, the quantum cascade laser (QCL) (13). A tunable QCL can optically pump almost any ro-vibrational transition  $J_L \rightarrow J_U$  of almost any molecule, thereby promoting population from lower level  $J_L$  into a virtually empty excited vibrational level (Fig. 1A). Sufficient pumping of upper level  $J_U$  by the QCL inverts the rotational transition  $J_U \rightarrow J_U - 1$  and induces this “direct” transition to lase at frequency  $\nu \approx 2BJ_U$ , where  $B$  is the rotational constant of the molecule. The rotational quantum number  $J_U$  is selected by the type of ro-vibrational transition excited by the QCL: for P-, Q-, and R-branch transitions,  $J_U = J_L -$

1,  $J_L$ , and  $J_L + 1$ , respectively. With sufficient QCL power, it is also possible to induce the “refilling” transition  $J_L + 1 \rightarrow J_L$  to lase, effectively doubling the number of laser lines for a given molecular gas.

The QCL-pumped molecular laser (QPML) is a universal concept: Almost any rotational transition from any molecule with a permanent dipole moment and a vapor pressure can be made to lase if a QCL can be precisely tuned across one of its IR bands. Terahertz lasing was recently reported on several NH<sub>3</sub> transitions near 1.0 THz (14), but we show theoretically and experimentally that the QPML tuning range can be much broader, a 200% fractional tunability covering the entire span of a molecule’s rotational spectrum, whose frequencies have been tabulated in several catalogs (15–17). The tuning range for several simple molecules (OCS, N<sub>2</sub>O, CH<sub>3</sub>F, HCN, and CO) is illustrated in Fig. 1B. Because  $B$  is inversely proportional to a principal moment of inertia of the molecule (18, 19), a low moment of inertia molecule like CO has sparser spacing, a broader tuning range, and a peak emission intensity at a high frequency, whereas a higher moment of inertia molecule like OCS has a denser spacing, a narrower tuning range, and a peak at a lower frequency. The number of available transitions increases as the molecular symmetry decreases and molecular mass increases.

Our comprehensive, physics-based multilevel model of the dominant collisional processes shows that OPFIR lasers operate most efficiently in compact cavities, with volumes more than 1000-fold smaller than conventional cavities (20–23). Our compact QPML configuration (Fig. 2A) includes aspects of the cavity design previously reported (20, 22): a 5-mm-diameter, 15-cm-long evacuated copper tube into which is inserted a copper rod rear reflector with a curved face that can be longitudinally scanned until the cavity mode overlaps the gain profile. The output coupler is a 1-mm-diameter pinhole in a flat front plate through which both the QCL and QPML beams propagate. The IR beam from the QCL is focused by a 15-cm-focal-length lens through a Brewster-angled ZnSe window to maximize power into the cavity (typically ~85%), while the terahertz beam diffracts through the pinhole and is refocused into a room-temperature power meter, a Schottky-diode detector, or a receiver operating in the frequency band of interest.

For a given QCL pump power, the terahertz power achievable by this room temperature laser depends on several factors. To ascertain the potential of a given molecular gas as a QPML, consider first the very low-pressure regime in which molecular collisions with the chamber walls occur more frequently than any intermolecular collisions, so a simple three-level model captures the salient behavior. Given that the ~1-MHz QCL linewidth (24) is much less

<sup>1</sup>Harvard John A. Paulson School of Engineering and Applied Sciences, Harvard University, Cambridge, MA 02138, USA. <sup>2</sup>Department of Mechanical Engineering, Massachusetts Institute of Technology, Cambridge, MA 02139, USA. <sup>3</sup>Department of Mathematics, Massachusetts Institute of Technology, Cambridge, MA 02139, USA. <sup>4</sup>Department of Physics, Massachusetts Institute of Technology, Cambridge, MA 02139, USA. <sup>5</sup>U.S. Army Combat Capabilities Development Command Aviation and Missile Center, Redstone Arsenal, AL 35898, USA. <sup>6</sup>Department of Physics, Duke University, Durham, NC 27708, USA.

\*Corresponding author. Email: everitt@phy.duke.edu (H.O.E.); capasso@seas.harvard.edu (F.C.)

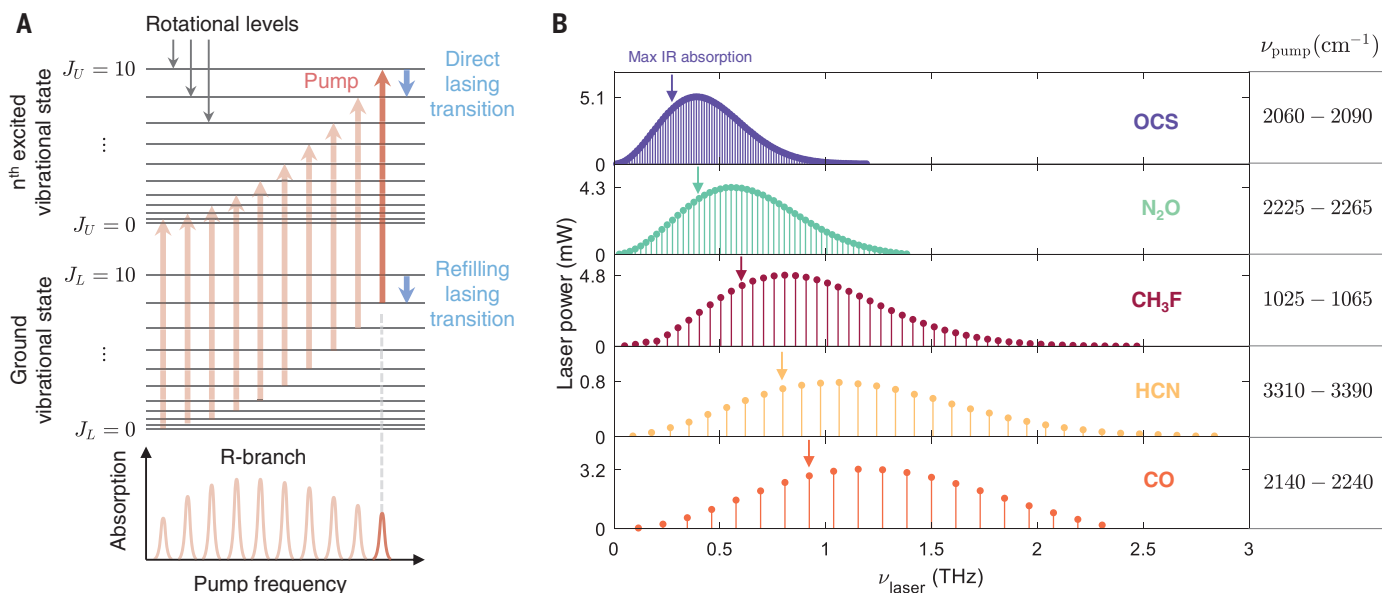


**Fig. 1. Universality of the quantum cascade laser-pumped molecular laser.**

(A) Diagram showing the rotational levels of a molecule for the ground and excited vibrational states. The red arrows illustrate R-branch transitions  $J_L \rightarrow J_U$  responsible for the IR absorption spectrum whose strength depends on the population of each  $J_L$ . The blue arrows indicate lasing transitions at frequencies corresponding to an inversion between two rotational states in the excited ("direct") or ground ("refilling") vibrational level. The frequency of the laser emission increases with increasing  $J_L$ . (B) Plot showing the QCL-pumped

molecular laser tuning range and power predicted by the simple model for direct transitions in 20 mTorr of various molecular gases in a compact cylindrical cavity pumped by a 0.25-W QCL: carbonyl sulfide (OCS), nitrous oxide ( $N_2O$ ), methyl fluoride ( $CH_3F$ ), hydrogen cyanide (HCN), and carbon monoxide (CO). The arrow indicates the laser transition corresponding to a pump transition from the rotational level with maximum population, illustrating how the Manley-Rowe effect skews the peak power to higher frequency. Also listed is the QCL tuning range required to pump the associated R-branch transitions.

than the ~50- to 150-MHz Doppler width of the IR molecular transition, a simple expression (25) gives the QPML power

$$P_{\text{THz}} = \frac{T}{4} \left( \frac{\nu_{\text{THz}}}{\nu_{\text{IR}}} \right) \left( \frac{\alpha_{\text{IR}}}{\alpha_{\text{cell}}} \right) [P_{\text{QCL}} - P_{\text{th}}] = \eta [P_{\text{QCL}} - P_{\text{th}}] \quad (1)$$

and identifies the essential parameters on which it depends at frequency  $\nu_{\text{THz}}$ . Here,  $\alpha_{\text{IR}}$  is the IR absorption coefficient of the gas molecule at the frequency  $\nu_{\text{IR}}$  to which the QCL is tuned,  $\alpha_{\text{cell}}$  captures the losses of the cavity,  $P_{\text{QCL}}$  is the QCL pumping power, and  $T$  is the front window transmission coefficient for the terahertz output. For our pinhole coupler with  $\nu_{\text{THz}} > c/2r_0$ ,  $T \approx (r_0/R_{\text{cell}})^2$ , where  $R_{\text{cell}}$  is the cavity radius and  $r_0$  is the radius of the output coupler. Combined, the factors before the square bracket in Eq. 1 constitute the power efficiency  $\eta$  of the QPML. The lasing threshold

$$P_{\text{th}} = \frac{\hbar^2 \nu_{\text{IR}}}{4\pi \alpha_{\text{IR}}} (\alpha_{\text{cell}} R_{\text{cell}}) \frac{u^2}{|\langle J_U - 1 | \mu | J_U \rangle|^2} \quad (2)$$

depends on many of the same parameters, as well as the average absolute molecular velocity  $u$  and the transition dipole matrix element of the rotational transition  $\langle J_U - 1 | \mu | J_U \rangle$ . As expected, the threshold increases with increasing cavity loss, but the dependence of  $P_{\text{th}}$  on

cell radius is more subtle because of the strong increase of  $\alpha_{\text{cell}}$  with decreasing  $R_{\text{cell}}$  due to ohmic loss (26) experienced by the modes of the hollow metal cavity. The threshold decreases for increasing dipole moment and decreasing  $\nu_{\text{IR}}$ , indicating that terahertz lasing is favored for strongly polar molecules with low frequency vibrational modes.

Equation 1 shows that the maximum power achievable by the QPML, often known as the Manley-Rowe limit (27), is determined by the ratio of the terahertz laser and IR pump frequencies  $\nu_{\text{THz}}/\nu_{\text{IR}}$ . Any vibrational band may be pumped by the QCL, but this Manley-Rowe limit (27) also recommends low frequency vibrational modes pumped by long-wavelength QCLs. Currently, more powerful QCLs are available at higher frequencies, so the selection of which vibrational mode to excite must be determined by its absorption strength, the Manley-Rowe factor, and the available QCL power.

Moreover, the Manley-Rowe factor indicates that the maximum power of the QPML grows with increasing laser frequency for a given QCL and vibrational band, in great contrast with electronic sources. This Manley-Rowe effect is tempered by the pressure-dependent population  $n_{J_L}$ , manifested in the IR absorption term  $\alpha_{\text{IR}}$ , available for the QCL to excite. One may simply look at the IR spectrum of a molecule to estimate how the power of the corresponding terahertz laser will depend on  $J_L$ . However,

the predicted power (Eq. 1) is proportional to the product of  $\alpha_{\text{IR}}$  and  $\nu_{\text{THz}}/\nu_{\text{IR}}$  and Fig. 1B confirms that the peak power occurs when the QCL pumps a transition with higher  $J_L$  than the peak of the IR band (where  $n_{J_L}$  is maximum) because of this Manley-Rowe effect.

The simple model of Eqs. 1 and 2 captures the molecular and cavity parameters essential for ascertaining how a given molecular gas will perform as a QCL-pumped terahertz laser. Table 1 and Fig. 1B summarize these behaviors for several candidate polar molecules, sorted by threshold pump power. The oblate symmetric top  $NH_3$  has recently been reported as a low threshold QPML near 1 THz (14), and the simple model reveals high power efficiency and large output power from many of these pure inversion transitions (25). However, the other molecules offer much greater tunability, in both range and spacing, and those with large  $\alpha_{\text{IR}}$  ( $NH_3$ ,  $CH_3F$ , OCS,  $N_2O$ , and CO) exhibit many lines with powers above 1 mW.

Because the simple, three-level model in Eqs. 1 and 2 is only valid at very low pressures where there is no collisional quenching of the laser inversion,  $P_{\text{THz}}$  is predicted to increase linearly with increasing pressure (through  $\alpha_{\text{IR}}$ ). This best-case approximation fails at higher pressures when intermolecular dipole-dipole, rotational-state randomizing, and velocity-randomizing collisions dominate the laser performance and quench the inversion in a manner that depends

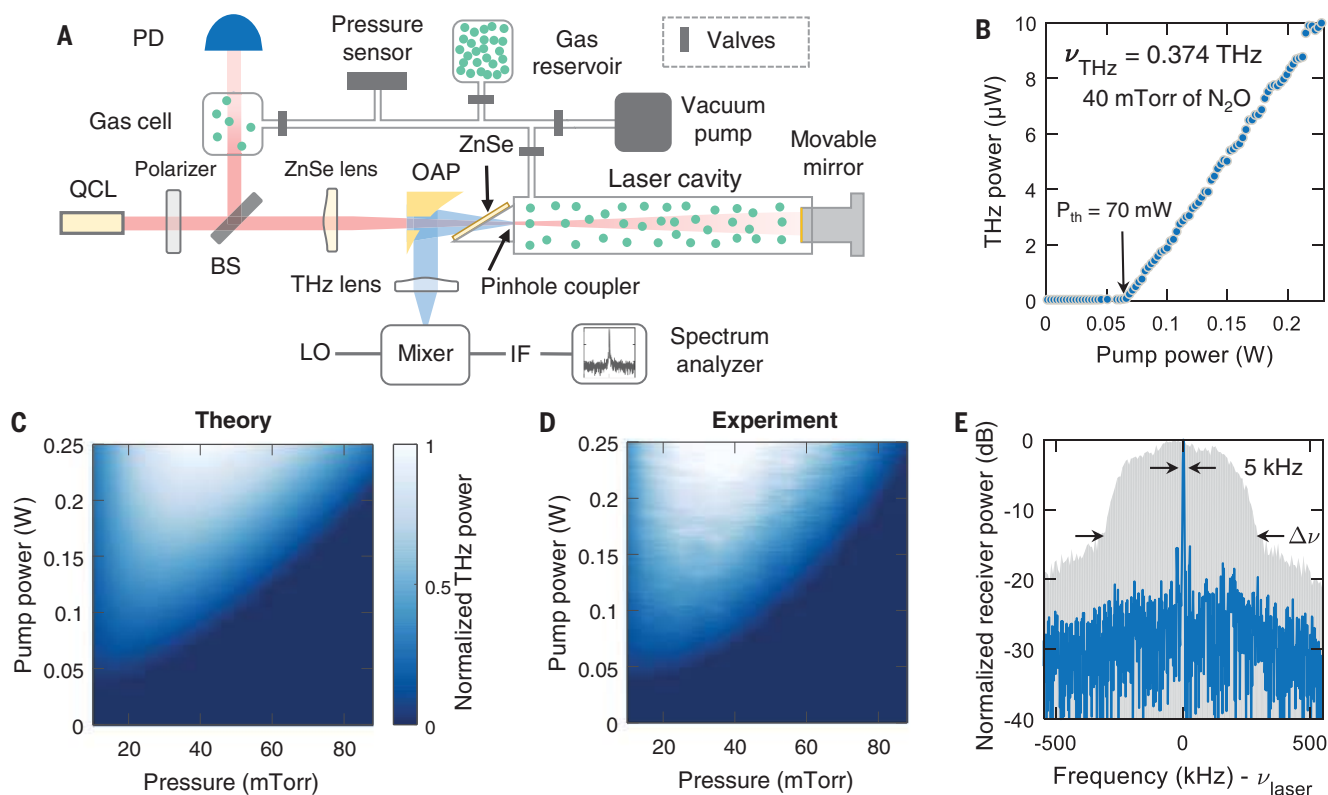


**Fig. 2. Experimental setup and results for the N<sub>2</sub>O molecular laser.**

(A) Experimental setup: IR light from a widely tunable QCL is tuned to pump a ro-vibrational transition and create a rotational population inversion. Light from the QCL is deflected by a 90%–10% beam splitter (BS) and transmitted through a gas cell so that the QCL may be tuned into coincidence with the vibrational transition by minimizing the transmitted intensity measured using a photodiode (PD). Light is coupled into the laser cavity through a ZnSe window at Brewster's angle and through a pinhole coupler in the cavity. A vacuum pump, pressure sensor, and gas reservoir are used to set the pressure in both the laser cavity and gas cell. The radiation emitted from the pinhole of the QPML is collected with the off-axis parabolic mirror (OAP), focused through a Teflon lens, and measured by a power meter, a detector, or a receiver that uses a frequency-multiplied local oscillator (LO) mixed with the signal to produce the

intermediate frequency (IF) measured by a spectrum analyzer. The pump power from the QCL is varied using a wire grid polarizer on a calcium fluoride substrate. The laser cavity is tuned into resonance with the lasing frequency by moving a copper mirror on a translation stage. (B) The measured output power of the QPML is plotted as a function of the IR pump power from the QCL. The threshold is  $P_{th} = 70$  mW. After accounting for losses in the collection of the emitted terahertz radiation, the maximum power is  $\sim 0.04$  mW, and  $\eta \approx 0.2$  mW/W at 40 mTorr for the  $J_U = 15 \rightarrow 14$  transition at 0.374 THz. Predicted (C) and measured (D) QPML normalized laser power as a function of gas pressure and QCL pump power for the same direct transition. (E) Emission spectrum of the laser (blue line) showing a linewidth of  $\leq 5$  kHz at 0.374 THz, corresponding to the  $J_U = 15 \rightarrow 14$  transition. The full tuning range of the QPML (broad gray feature) is achieved by varying the cavity length.

on collision cross sections that may not be known. We have previously reported a comprehensive, multilevel model that thoroughly captures these behaviors, finding that the IR-to-terahertz photon conversion efficiency of an optimized CH<sub>3</sub>F OPFIR laser may exceed 30% (23). This model has been adapted to predict the performance of QPMLs as a function of  $P_{QCL}$  and pressure (25).

To illustrate the performance and tunability of a compact QPML, we chose nitrous oxide (N<sub>2</sub>O), whose  $\nu_3$  vibrational mode falls within the 2119 to 2342 cm<sup>-1</sup> tuning range of our 320-mW QCL. The spacings of the N<sub>2</sub>O lasing transitions are  $\sim 2B_{N_2O} = 25.1$  GHz, and the frequency span over which this QPML may be tuned is  $\sim 1.5$  THz. QCL frequency tuning was accomplished by monitoring the IR signal transmitted through a separate 15-cm gas cell

containing 50 mTorr of N<sub>2</sub>O using a HgCdTe detector. The QCL frequency was tuned by precise temperature control until molecular absorption minimized the transmitted IR power (Fig. 2A). Here, we will refer to lasing transitions (both direct and refilling) by the quantum number  $J_L$  of the lower level drained by the IR pump.

We observed lasing for all 29 direct lasing transitions (Fig. 3A), as well as eight refilling transitions (Fig. 3B), between 0.251 and 0.955 THz (corresponding to  $9 \leq J_L \leq 37$ ) by exciting each R-branch  $\nu_3$  ro-vibrational transition over a QCL tuning range of 2231 to 2250 cm<sup>-1</sup>. Refilling transitions and direct transitions corresponding to the same  $J_L$  exhibit slightly different frequencies owing to different  $B$  rotational constants for the ground and excited vibrational states. Lasing below 0.251 THz could

not be observed because it occurred below the radiation-suppressing cutoff frequency of the pinhole output coupler. For most transitions, we measured the strength of the laser emission as a function of pressure for maximum QCL pumping power, and in some cases we also measured the laser emission as a function of QCL pumping power (see Fig. 2B for  $J_L = 14$ ). From these measurements, we were able to obtain the threshold power  $P_{th}$  and power efficiency  $\eta$  of many laser lines (25), providing critical information for ascertaining the molecular dipole-dipole and thermalizing gas kinetic collisional cross sections needed in the comprehensive model (22, 23, 28).

We also used heterodyne receivers operating between 0.300 and 0.775 THz to measure the spectrum of these laser transitions (see Fig. 2E for the recovered line at  $\nu_{THz} = 0.374$  THz).

**Table 1. Predicted QPML power (Eq. 1) and QCL threshold pump power (Eq. 2) for the highest power lasing transition of nine candidate laser molecules at 20 mTorr.** Assumes a 0.25-W QCL pumping through a 1-mm-diameter pinhole output coupler into a 5-mm-diameter cylindrical laser cavity (loss =  $0.06 \text{ m}^{-1}$ ) containing the molecular gas with dipole moment  $\mu$ . With optimized pressure, even higher power is achievable (23).

Molecule	$J_L$ (peak)	$\nu_{\text{THz}}$ (THz)	$P_{\text{THz}}$ (mW)	$P_{\text{th}}$ (mW)	$\eta$ (mW/W)	$\mu$ (D)	$\nu_{\text{IR}}$ ( $\text{cm}^{-1}$ )	$\alpha_{\text{IR}}$ ( $\text{m}^{-1}$ )
CH <sub>3</sub> F	15	0.806	4.8	0.041	19.2	1.85	1072.774	4.59
NH <sub>3</sub>	3	1.073	16.7	0.056	66.6	1.46	967.346	10.8
OCS	31	0.389	5.2	0.069	20.5	0.72	2073.894	19.6
HCN	11	1.063	0.8	0.164	3.11	2.98	1447.962	0.76
H <sub>2</sub> CO	13	1.087	0.8	0.218	3.28	2.33	1776.861	0.96
CH <sub>3</sub> <sup>35</sup> Cl	20	0.558	0.04	2.42	0.14	1.90	1459.582	0.07
N <sub>2</sub> O	21	0.553	4.3	3.14	17.4	0.17	2240.439	12.7
CH <sub>3</sub> OH	15	2.523	0.2	4.88	0.92	1.41	1031.477	0.07
CO	9	1.153	3.2	27.2	14.5	0.12	2179.772	4.93

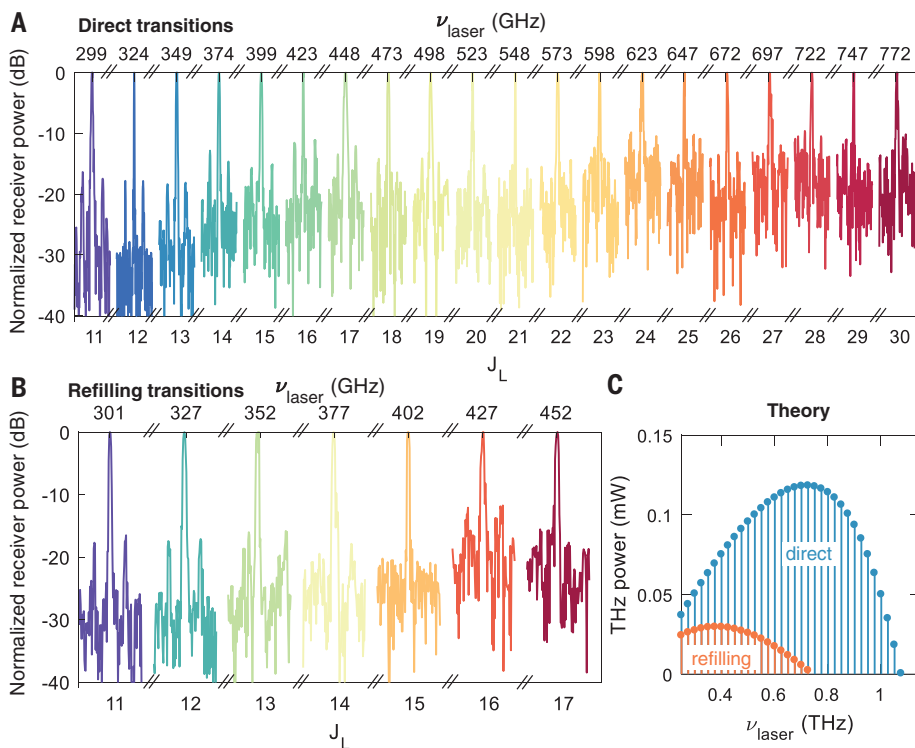


**Fig. 3. Tunability of the optically pumped N<sub>2</sub>O laser.** Emission spectra of the laser were measured as the QCL pump laser was tuned to different IR transitions of N<sub>2</sub>O. The x axes show the measured emission frequency and the associated quantum number  $J_L$  of the lower level of the pumped R-branch transition. The QCL power was maximal (up to 0.25 W coupled in the cavity), and the pressure was 40 mTorr for direct transitions and 20 mTorr for refilling transitions. (A) Measured spectra of direct transitions with  $J_L$  from 11 to 30. (B) Measured spectra of refilling transitions with  $J_L$  from 11 to 17. (C) The output power of the laser predicted by the comprehensive model (23) using the deduced collisional parameters of N<sub>2</sub>O and the estimated cavity losses, plotted as a function of frequency for the optimal pressure.

The instantaneous linewidths were  $<1$  kHz, but because of frequency jitter the effective linewidths were typically 3 to 6 kHz. Other measured lines are shown in Fig. 3, A and B, over a 200-kHz span. We were able to dem-

onstrate frequency tuning of the laser across its full Doppler-broadened gain bandwidth by precisely adjusting the cavity length with a motorized micrometer. The broad feature (gray curve) in Fig. 2E envelopes the range

of individual frequencies over which the laser was tuned while keeping the pump laser at a constant power and frequency. Importantly, the QPML frequency was quite stable (routinely  $<10$  kHz) while freely running and could be made even more stable through active frequency stabilization of the QCL (29) and the laser cavity (30).

Constrained by these experimental measurements of terahertz power as a function of pressure and pump power, our comprehensive theoretical model (23) was able to estimate the collisional cross sections and predict the optimal performance of the laser. The dipole-dipole collisional cross section was estimated to be  $35 \text{ \AA}^2$ , well within the expected range (25), while the cavity loss ( $\alpha = 0.3 \text{ m}^{-1}$  at 374 GHz) was estimated to be five times higher than the theoretical minimum (25). Figure 2, C and D, respectively, reveal the excellent agreement between the predicted and measured output terahertz power for  $J_L = 14$  as a function of N<sub>2</sub>O pressure and QCL pump power. The model predicts, and measurements confirm, that the optimal and maximum pressure for laser operation increases with increasing  $J_L$  (25), a consequence of the increasing Doppler width of the gain profile with increasing laser frequency.

The comprehensive model was used to predict the expected laser power for each transition at its optimal gas pressure, and Fig. 3C shows that the direct lasing transition with maximum power occurs not for  $J_L = 15$ , where  $n_{J_L}$  is largest, but for  $J_L = 28$  because of the Manley-Rowe effect. While the output power increased as a function of the frequency, the signal-to-noise ratio in the heterodyne measurement (Fig. 3, A and B) was limited by the decreasing efficiency of the electronic subterahertz source. An emitted power of 69  $\mu\text{W}$  was predicted for the  $J_L = 14$ ,  $\nu_{\text{THz}} = 0.374$  THz direct transition. Although we measured only 10  $\mu\text{W}$  (Fig. 2B), our power measurements underestimate the emitted power by at least a factor of four, for reasons including significant diffraction of the emitted terahertz beam beyond the collection optics, absorption and reflection by the ZnSe Brewster window and Teflon lens, and use of the power meter at the edge of its calibrated range.

Like traditional OPFIR lasers, QPMLs exhibit high brightness temperatures  $T_b = Ic^2 / (2k\nu_{\text{THz}}^2 \Delta\nu) > 10^{14} \text{ K}$  for laser radiance  $I = 1 \text{ mW}\cdot\text{cm}^{-2}\cdot\text{sr}^{-1}$  (where  $k$  is the Boltzmann constant,  $c$  is the speed of light, and  $\Delta\nu = 1$  kHz the linewidth). Because our theoretical models and experimental demonstrations with N<sub>2</sub>O confirm the universal concept of a terahertz molecular laser source broadly tunable across its entire rotational manifold when pumped by a continuously tunable QCL, the outlook for QPMLs is indeed very bright.

## REFERENCES AND NOTES

1. T. Nagatsuma, G. Ducournau, C. C. Renaud, *Nat. Photonics* **10**, 371–379 (2016).
2. R. A. Lewis, *J. Phys. D Appl. Phys.* **47**, 374001 (2014).
3. A. Maestrini *et al.*, *IEEE Trans. Microw. Theory Tech.* **58**, 1925–1932 (2010).
4. J. H. Booske *et al.*, *IEEE Trans. Terahertz Sci. Technol.* **1**, 54–75 (2011).
5. Y. Shen, P. Upadhyaya, E. Linfield, H. Beere, A. Davies, *Appl. Phys. Lett.* **83**, 3117–3119 (2003).
6. K. McIntosh *et al.*, *Appl. Phys. Lett.* **67**, 3844–3846 (1995).
7. K. Evenson, D. Jennings, F. Petersen, *Appl. Phys. Lett.* **44**, 576–578 (1984).
8. M. Inguscio, P. D. Natale, L. Veseth, *Comments At. Mol. Phys.* **30**, 3 (1994).
9. R. Köhler *et al.*, *Nature* **417**, 156–159 (2002).
10. L. Bosco *et al.*, *Appl. Phys. Lett.* **115**, 010601 (2019).
11. C. A. Curwen, J. L. Reno, B. S. Williams, *Nat. Photonics* 10.1038/s41566-019-0518-z (2019).
12. T. Chang, T. Bridges, E. Burkhardt, *Appl. Phys. Lett.* **17**, 249–251 (1970).
13. J. Faist *et al.*, *Science* **264**, 553–556 (1994).
14. A. Pagies, G. Ducournau, J.-F. Lampin, *APL Photonics* **1**, 031302 (2016).
15. I. Gordon *et al.*, *J. Quant. Spectrosc. Radiat. Transf.* **203**, 3–69 (2017).
16. JPL Molecular Spectroscopy Database (2017); <https://spec.jpl.nasa.gov/>.
17. Splatalogue Database for Astronomical Spectroscopy (2007); [www.cv.nrao.edu/php/splat/](http://www.cv.nrao.edu/php/splat/).
18. C. Townes, A. L. Schawlow, *Microwave Spectroscopy* (Dover Publications, 1995).
19. W. Gordy, R. L. Cook, *Microwave Molecular Spectroscopy* (Wiley-Interscience, 1984).
20. H. O. Everitt, D. D. Skatrud, F. C. De Lucia, *Appl. Phys. Lett.* **49**, 995–997 (1986).
21. R. McCormick, H. Everitt, F. De Lucia, D. Skatrud, *IEEE J. Quantum Electron.* **23**, 2069–2077 (1987).
22. S.-L. Chua *et al.*, *Opt. Express* **19**, 7513–7529 (2011).
23. F. Wang *et al.*, *Proc. Natl. Acad. Sci. U.S.A.* **115**, 6614–6619 (2018).
24. K. Knabe *et al.*, *Opt. Express* **20**, 12432–12442 (2012).
25. See supplementary materials.
26. R. Bansal, *Fundamentals of Engineering Electromagnetics* (CRC Press, 2006).
27. J. Manley, H. Rowe, *Proceedings of the IRE* **44**, 904–913 (1956).
28. H. O. Everitt, F. C. De Lucia, *Adv. At. Mol. Opt. Phys.* **35**, 331–400 (1995).
29. R. M. Williams *et al.*, *Opt. Lett.* **24**, 1844–1846 (1999).
30. R. L. Crownover, H. O. Everitt, F. C. De Lucia, D. D. Skatrud, *Appl. Phys. Lett.* **57**, 2882–2884 (1990).

## ACKNOWLEDGMENTS

The authors acknowledge F. De Lucia (Ohio State Univ.), T. Goyette (U. Mass Lowell), and S. Paolini (Harvard CNS) for helpful advice.

**Funding:** This work was partially supported by the U.S. Army

Research Office (W911NF-19-2-0168 and W911NF-13-D-0001) and by the National Science Foundation (NSF; ECCS-1614631) and its Materials Research Science and Engineering Center Program (DMR-1419807). Some of this work was performed at the Harvard University Center for Nanoscale Systems (CNS), part of the NSF-supported National Nanotechnology Coordinated Infrastructure Network (ECCS-1541959). Any opinions, findings, conclusions, or recommendations expressed in this material are those of the authors and do not necessarily reflect the views of the Assistant Secretary of Defense for Research and Engineering or of the NSF. **Author contributions:** H.O.E. conceived of the QPML concept; developed the theory with F.W. and S.G.J.; and demonstrated its operation with P.C., A.A., M.P., and F.C. All authors contributed to the writing of the manuscript. **Competing interests:** A provisional patent application has been filed on the subject of this work. **Data and materials availability:** All data are available in the manuscript or the supplementary materials.

## SUPPLEMENTARY MATERIALS

[science.sciencemag.org/content/366/6467/856/suppl/DC1](http://science.sciencemag.org/content/366/6467/856/suppl/DC1)  
Materials and Methods  
Supplementary Text  
Figs. S1 to S8  
References (31–36)

15 August 2019; accepted 21 October 2019  
10.1126/science.aay8683



## Supplementary Materials for **Widely tunable compact terahertz gas lasers**

Paul Chevalier, Arman Armizhan, Fan Wang, Marco Piccardo, Steven G. Johnson,  
Federico Capasso\*, Henry O. Everitt\*

\*Corresponding author. Email: everitt@phy.duke.edu (H.O.E.); capasso@seas.harvard.edu (F.C.)

Published 15 November 2019, *Science* **366**, 856 (2019)  
DOI: 10.1126/science.aay8683

**This PDF file includes:**

Materials and Methods  
Supplementary Text  
Figs. S1 to S8  
References

## CONTENTS

I. Materials and Methods	2
A. Tuning the QCL emission into the gas absorption line	2
B. Controlling the pressure inside the THz laser cavity	3
C. Measuring the THz laser output	3
II. Theoretical Modeling	4
III. Determination of $\sigma_{DD}$ and other parameters	5
IV. Output and threshold power for different transitions	6
V. Analytical derivation of threshold and output powers	7
A. Pump threshold	8
B. THz output power	9
VI. Using ammonia ( $\text{NH}_3$ ) as a QPML gain medium	9
References	11

## I. MATERIALS AND METHODS

### A. Tuning the QCL emission into the gas absorption line

External-Cavity (EC)-QCLs rely on a diffraction grating mounted on a precisely controlled actuator (piezo-electric, stepper-motor, voice-coil actuator). The laser device used in this paper (Daylight Solutions HHG 41045), is factory calibrated for grating tuning of the emission, but this tuning is discrete and typically has a resolution of  $0.1 \text{ cm}^{-1}$ . According to the manufacturer specifications, the target emission wavenumber and the actual emission wavenumber may differ by up to  $1 \text{ cm}^{-1}$ . Once the grating is tuned to a desired position, continuous tuning can occur by changing the temperature of the laser. For the experiments described here, tuning into an absorption line was performed as follows: a line is selected and the grating of the EC-QCL is tuned close to the HITRAN value for the transition, then the QCL temperature is cycled between 17 and  $22^\circ\text{C}$  while the transmitted intensity through the gas cell is monitored by a Vigo PV-106 HgCdTe detector. If during this cycling of the temperature a strong absorption feature was observed, the QCL temperature was finely adjusted in order to minimize the transmitted intensity. The emission wavenumber of the QCL was then measured on the FTIR and compared with HITRAN data to confirm that the targeted transition was effectively selected. If during the cycling of the QCL temperature no absorption feature was seen, then the grating was tuned by increments of  $0.1 \text{ cm}^{-1}$  until an absorption feature was observed.

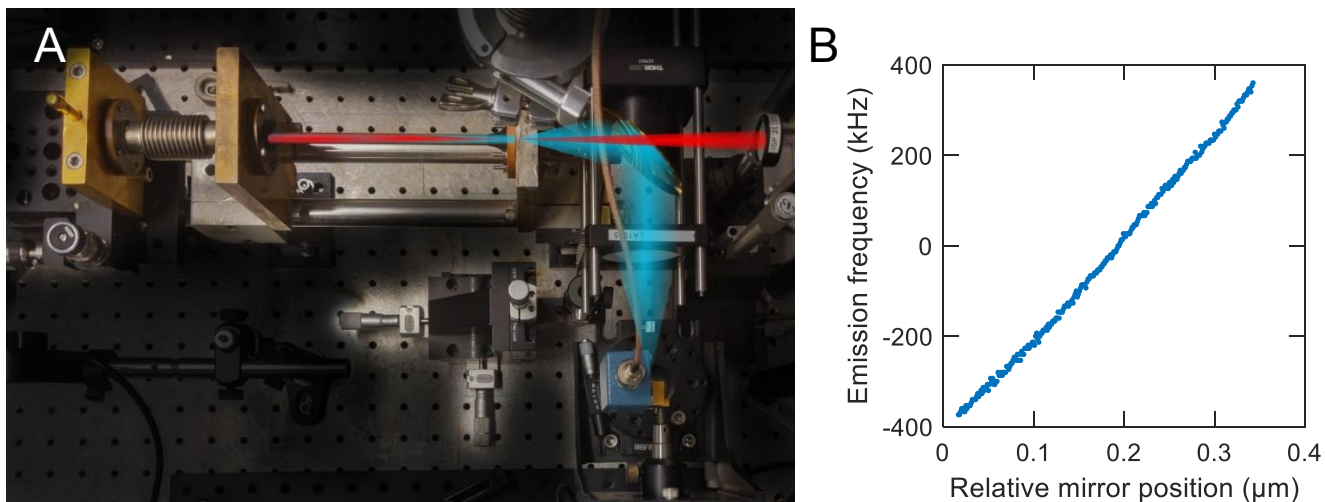


Figure S1. **A** Photograph of the experimental setup showing the different components of the laser cavity, the path of the QCL beam (red), and how the output light (blue) is collected. **B** Plot of the measured relative emission frequency of the THz gas laser as a function of the back-mirror position for  $J_L = 10$ , ( $\nu_{\text{THz}} \approx 0.299$  THz).

### B. Controlling the pressure inside the THz laser cavity

The operating pressure range of the laser (Fig. S1A) lies between 10 mTorr and 100 mTorr (or 1.3 Pa to 13 Pa). To measure such low pressure levels in the cavity we use a Pirani pressure gauge (Alcatel sensor AP1004 and controller ACR1000) which has a resolution of  $10^{-5}$  Torr and an accuracy of  $10^{-3}$  Torr. To fill the cavity with a specific amount of gas, first a high vacuum (pressure below  $10^{-5}$  Torr) is achieved in the cavity by using a Varian DS402 rough pump and a Varian V-70LP Turbo pump. A sample tube connected to the vacuum manifold with a valve and containing a few Torr of pure nitrous oxide at atmospheric pressure is cooled down by a bath of liquid nitrogen (see schematic in Fig. 2A of the manuscript). Once high vacuum is reached in the cavity, nitrous oxide is introduced in the cavity by closing the vacuum pump valve, opening the valve of the sample tube and warming the tube and its contents. Since the liquid nitrogen bath has initially completely solidified the nitrous oxide in the tube, the sublimation of nitrous oxide will progressively increase the pressure in the cavity. The valve of the sample tube is closed when the proper pressure is reached in the cavity. To reduce the pressure in the cavity, nitrous oxide can be recycled into the sample tube by immersing it again in a bath of liquid nitrogen. This method allows for a slow rise of the pressure in the cavity and for reusing of the gas between experiments. Other methods, such as using a variable leak valve, would allow for precise pressure control but would not allow for reusing of the gas.

### C. Measuring the THz laser output

Once the QCL was tuned into an absorption line and its emission frequency was confirmed, IR radiation passed through a hole in an off-axis parabolic mirror, through a ZnSe window at Brewster's angle, and through a 1 mm diameter pinhole into the laser cavity containing the molecular gas. Then, the back-mirror of the THz cavity was moved until lasing began and THz intensity was measured by the detector. Schottky diode detectors used for that purpose were Virginia Diodes, Inc. Zero Bias detectors (ZBD) with waveguide sizes WR3.4, WR2.2, WR1.5, WR1.2, and WR1.0 depending on the targeted emission frequency. The signal from the detector was amplified using a low-noise voltage amplifier (Stanford research SR560). The amplification factor was typically set between 5000 and 20,000.

The power output of the laser was measured using a calibrated power meter THZ5B-BL-DZ-D0 from Gentec electro-optics.

The spectral lines of the THz laser were measured using a receiver and mixer from Virginia Diodes. The WR2.2 receiver, covering 300 GHz to 550 GHz operated with a multiplier factor of 36 with a local oscillator (LO) power of 10 dBm. The WR1.5 receiver, covering 550 GHz to 775 GHz operated with a multiplier factor of 54 with an LO power of 15 dBm. The signal generator providing the LO signal was a Hittite HMC-T2240. The intermediate frequency (IF) was measured on an Agilent E4448A spectrum analyzer.

To obtain the molecular gain profile of the THz laser at a given pumped transition, the emission frequency of the laser was measured for different positions of the back-mirror. The free spectral range of the 15 cm long Fabry-Perot cavity is of the order of 1 GHz. As the relative position of the mirror increases, the length of the cavity decreases and the cavity mode ( $\approx 10 - 100$  MHz

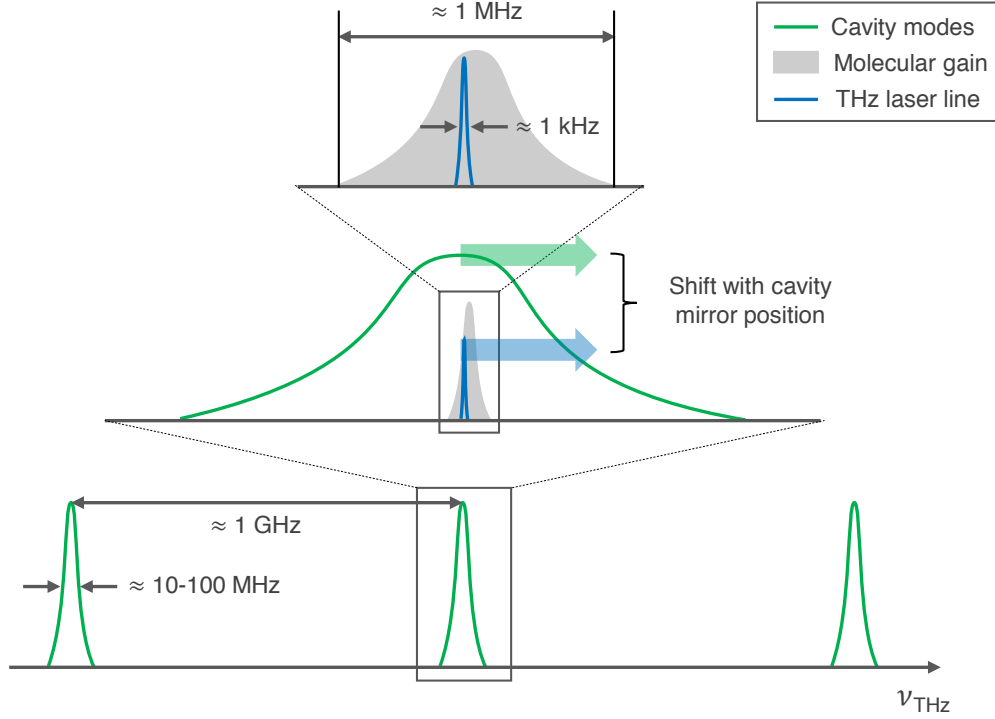


Figure S2. Schematic showing the tuning range of the THz laser for a given pumped transition. As the back-mirror of the gas cavity is translated, the free spectral range of the resonator is modified, resulting in a shift of the cavity modes. This in turn causes the emission frequency of the laser to shift within the frequency range of the molecular gain profile.

linewidth) is shifted toward higher frequencies (Fig. S2). This in turn shifts the laser frequency, to minimize the cavity losses and maximize the gain. In Fig. S1B, the emission frequency of the laser is plotted as a function of the position of the back-mirror. Since laser emission can only happen while a cavity mode overlaps with the gain profile of the pumped transition, this measurement gives the tuning range of the QPML ( $\approx 1$  MHz) for a given transition, as shown by the grey curve of Fig. 2E of the manuscript.

## II. THEORETICAL MODELING

In the main text, a simple model is presented to describe the lasing behavior at low pressures with negligible intermolecular collisional transition rates. In order to fully understand the lasing behavior across all pressures, we have developed a more comprehensive model that thoroughly captures the collisional physics and can accurately predict the performance of QCL-pumped molecular lasers (QPMLs) [23]. In the model, rate equations of the population density of vibrational and rotational levels are solved numerically, and then the THz output power is computed based on the population inversions obtained from the rate equations when the QCL pump creates nonequilibrium populations.

For the  $\text{N}_2\text{O}$  laser, the model includes  $J_L + 8$  rotational levels and the 10 lowest energy vibrational levels. The rate equations for the *rotational levels* are

$$\begin{aligned} \frac{dN_\ell(v, \mathbf{r}, t)}{dt} = & \sum_{\ell'=\ell\pm 1} [-\gamma_{\ell\ell'} N_\ell(v, \mathbf{r}, t) + \gamma_{\ell'\ell} N_{\ell'}(v, \mathbf{r}, t)] \\ & - \gamma_{\text{SPT}} N_\ell(v, \mathbf{r}, t) + R_{\text{pump}}(v, \mathbf{r}, t) + D\nabla^2 N_\ell(v, \mathbf{r}, t) \end{aligned} \quad (\text{S1})$$

where  $N_\ell(v, \mathbf{r}, t)$  is the nonthermal population density for rotational level  $\ell$  with axial velocity  $v$  along the pump beam direction, at position  $\mathbf{r}$ , and at time  $t$ ,  $\gamma_{\ell\ell'}$  is the dipole–dipole collisional transition rate. The thermal population density is calculated separately as part of the total population of a vibrational level, as described below. From the selection rules,  $\ell'$  can only be  $\ell \pm 1$ . The transition rate is determined by  $\gamma_{\ell\ell'} = n_{\text{tot}} \langle v_{\text{rel}} \rangle \sigma \rho_{\ell\ell'}$ , where  $n_{\text{tot}}$  is the total molecular population density,  $\langle v_{\text{rel}} \rangle$  is the thermally averaged relative velocity,  $\rho_{\ell\ell'}$  is the appropriate branching ratio with Boltzmann factor, and  $\sigma$  is the collisional cross section for the transition. In gas phase OPFIR lasers, the dominant collisional process is mediated by the dipole–dipole interaction, so that  $\sigma \approx \sigma_{\text{DD}}$ . In the second line of Eq. (S1),  $(-\gamma_{\text{SPT}} N_\ell)$  describes the thermalization transition of rotational

level  $\ell$  into its vibrational mode due to low energy collisions. The thermalization rate  $\gamma_{\text{SPT}}$  is computed from the gas kinetic cross section as  $\sigma_{\text{GK}} = 15\text{\AA}^2$ .  $R_{\text{pump}}$  describes the pump transition  $J_L \rightarrow J_U$  thoroughly. It includes inhomogeneous broadening from different velocity subclasses with the Doppler effect, pressure broadening with HWHM equal to 4.0MHz/Torr, velocity-dependent saturation, and the multiple round-trips inside the cavity. The linewidth of the pump EC-QCL used in experiments is typically a few MHz. The detailed formula for  $R_{\text{pump}}$  can be found in Ref. 23. Diffusion is also included in the last term of Eq. (S1).

Similarly, the rate equations for the *vibrational levels* are

$$\begin{aligned} \frac{dN_p(v, \mathbf{r}, t)}{dt} = & \sum_{p'=p\pm 1} [-\gamma_{pp'} N_p(v, \mathbf{r}, t) + \gamma_{p'p} N_{p'}(v, \mathbf{r}, t)] \\ & + \Sigma_\ell \gamma_{\text{SPT}} \int dv N_\ell(v, \mathbf{r}, t) + D \nabla^2 N_p(v, \mathbf{r}, t) \end{aligned} \quad (\text{S2})$$

in which  $\gamma_{pp'}$  is the transition rate between vibrational levels  $p \rightarrow p'$  and is assumed proportional to the gas kinetic cross section  $\sigma_{\text{GK}}$  and Boltzmann factor  $\exp(-\Delta E_{pp'}/k_B T)$ , where  $\Delta E_{pp'}$  is the vibrational energy difference between  $p$  and  $p'$ . The last two terms describe the thermalization from rotational levels to vibrational levels as well as diffusion. The thermal population of a given rotational state is simply that state's fraction of the total thermal population in the corresponding vibrational level.

Molecule-wall collisions are modeled by a reaction boundary condition [23] so that wall collisions thermalize the vibrational levels and redistribute the molecules into all possible levels with a Boltzmann distribution at room temperature (300K). The ground vibrational state has the largest occupation probability.

We obtain the steady state by setting  $dN/dt = 0$ . These nonlinear rate equations are discretized and solved numerically by fixed-point iteration with Anderson Acceleration [23]. At each iteration step, MUMPS (MUltifrontal Massively Parallel sparse direct Solver [31]) is used for factorizing the sparse matrix.

THz output power is then obtained by matching the cavity loss  $\alpha_{\text{cell}}$  with the THz gain. In particular, the cavity loss includes Ohmic loss  $\alpha_{\text{Ohmic}}$  and transmission loss through the front window  $\alpha_{\text{trans}}$ . Ohmic loss can be expressed analytically for the modes of a hollow metal waveguide, which increases strongly with decreasing radius [26]. The transmission loss is estimated by  $\alpha_{\text{trans}} = -\log(1-T)/2L$ , where  $T$  is the front window transmission coefficient, and  $L$  is the cavity length. The gain coefficient is obtained by integrating contributions from all velocity subclasses. Detailed discussions and computational treatments can be found in Ref. 23.

### III. DETERMINATION OF $\sigma_{\text{DD}}$ AND OTHER PARAMETERS

Unlike widely-studied  $\text{CH}_3\text{F}$ , whose collisional parameters are experimentally well known [20, 21], many important collisional cross sections of  $\text{N}_2\text{O}$  are unknown, such as the most important  $\sigma_{\text{DD}}$  (dipole-dipole collisions). However, thanks to the completeness of our OPFIR model, we can use our experimental measurements of QMPL power as a function of pressure and QCL pump power to extract a few key unknowns by a fitting procedure. In particular, we use experimental fits to recover the dipole-dipole cross section  $\sigma_{\text{DD}}$ , the cavity loss (since the alignment and other geometric factors were imperfectly known for our cavity), and the QCL linewidth. Our numerical modeling finds that the output power is insensitive to the gas kinetic collisional cross section, so  $\sigma_{\text{GK}}$  is fixed as  $15\text{\AA}^2$ , well within the expected range. Once these parameters were obtained, we could then proceed to use the model to predict other lasing behaviors and to identify the optimal cavity and operating regime.

Figure S3 shows the threshold power for the  $J_L = 14$  direct lasing transition as a function of pressure for both experimental measurements (blue circles) and theoretical modeling (dashed lines) with different dipole-dipole cross sections  $\sigma_{\text{DD}} = 25\text{\AA}^2$ ,  $35\text{\AA}^2$ , and  $45\text{\AA}^2$ . A reasonable range for  $\sigma_{\text{DD}}$  can be estimated by assuming  $\sigma_{\text{DD}}$  proportional to the dipole moment  $\mu$  of the molecule. Consider  $\mu_{\text{N}_2\text{O}} = 0.17$  D,  $\mu_{\text{CH}_3\text{F}} = 1.8$  D, and  $\sigma_{\text{DD}}^{\text{CH}_3\text{F}} = 320\text{\AA}^2$ , so  $\sigma_{\text{DD}}^{\text{N}_2\text{O}} \approx \sigma_{\text{DD}}^{\text{CH}_3\text{F}} \frac{\mu_{\text{N}_2\text{O}}}{\mu_{\text{CH}_3\text{F}}} = 30\text{\AA}^2$ . Fig. S3 shows that  $\sigma_{\text{DD}} = 35\text{\AA}^2$  gives the best agreement with experiments, which is also within the reasonable range. The cavity loss from the fitting is  $0.3\text{ m}^{-1}$ , which is about 5 times larger than an ideal cylindrical cavity operating on the  $\text{TE}_{01}$  mode. In principle, cavity loss can be computed with the exact cavity geometry and cavity mode. However, our current cavity has poor alignment using a concave back mirror with focal length about 2-3 cm, which easily couples the lasing mode to other cavity modes. In addition, the front pinhole coupler has a curved taper from the 1 mm diameter exit to the 5 mm diameter cavity, and this taper also contributes to mode mixing while suppressing long wavelength emission below cutoff. The QCL linewidth is fitted as 2 MHz to match Fig. 2C with Fig. 2D in the main text, a value that is well within the range previously reported for EC-QCLs [24].

Using the obtained collisional parameters, the theory-experiment match for  $J_L = 31$  is also presented in Fig. S4. The agreement between theoretical modeling and experiments confirms the correctness of the deduced collisional cross sections and QCL linewidth. Only the cavity loss had to be adjusted, increased to  $0.46\text{ m}^{-1}$  at this higher frequency to obtain good agreement. A frequency-dependent cavity loss is expected because of the increasing number of modes above cutoff at higher frequencies, which are coupled more easily to the lasing mode by the concave back plunger in our cavity with increasing  $J_L$  and lasing frequency. There is potential for improving the cavity design with a different geometry mirror or metasurface.

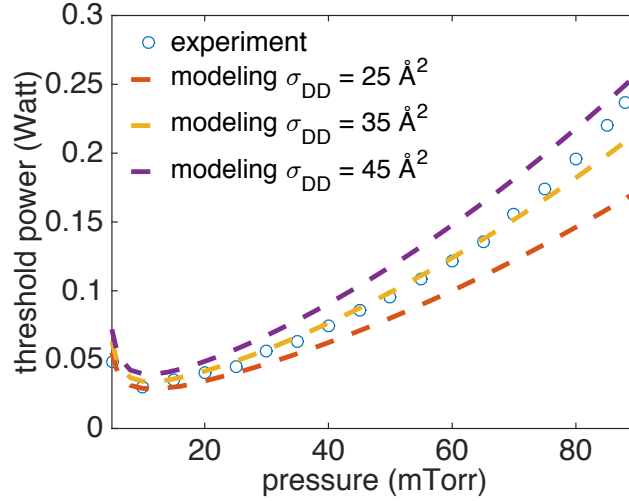


Figure S3. Threshold power for the direct lasing transition as a function of pressure for  $J_L = 14$  or  $\nu = 374$  GHz. Results from experimental measurement (blue circles) and theoretical modeling (dashed lines) with different values of  $\sigma_{DD} = 25 \text{ \AA}^2$ ,  $35 \text{ \AA}^2$ , and  $45 \text{ \AA}^2$  are compared. In the model, the cavity loss is a fitting parameter ( $0.3 \text{ m}^{-1}$ ). The results imply that the dipole–dipole cross section of  $\text{N}_2\text{O}$  is  $\sigma_{DD} = 35 \text{ \AA}^2$ .

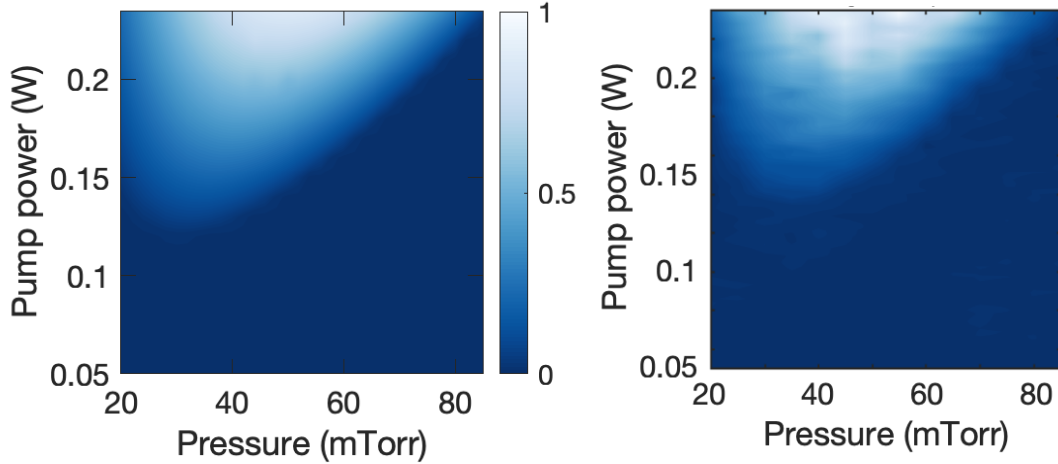


Figure S4. Contour plot of the THz output power from the  $J_L = 31$  direct lasing transition at  $\nu_{\text{THz}} = 0.797$  THz as a function of pressure and pump power. The theoretical prediction (left) matches the experimental measurement (right) very well using the previously obtained dipole–dipole collisional cross section  $\sigma_{DD} = 35 \text{ \AA}^2$ , and QCL linewidth of 2 MHz. The cavity loss is the only fitting parameter ( $0.46 \text{ m}^{-1}$ ).

#### IV. OUTPUT AND THRESHOLD POWER FOR DIFFERENT TRANSITIONS

Fig. S3 indicates that the pump threshold power increases with pressure, but this doesn't imply higher powers at lower pressures, because only a limited pressure-broadened velocity subclass fraction of the  $J_L$  population can be pumped. The optimal pressure with the highest output power occurs in between, as shown in Fig. S5 for both direct and refilling lasing with  $J_L = 6$  ( $\sim 175$  GHz) to  $J_L = 41$  ( $\sim 1.05$  THz). The peak powers for different transitions at the optimal pressures are plotted in the main text Fig. 3C. The comprehensive model predicts the direct transition with  $J_L = 28$  produces the highest power. This is slightly different from the simple model prediction where the peak power appears for the transition with  $J_L = 21$ , as shown in Fig. 1B. The discrepancy is caused by the low pressure limitation of the simple model. In Fig. 1B, we fixed the gas pressure at 20 mTorr within the valid region of the simple model, while the comprehensive model implies that the optimal pressures are typically above 40 mTorr. In fact, Fig. S5A confirms that at 20 mTorr the transition with  $J_L = 21$  has the highest power. Furthermore, lasing from direct inversion operates at higher pressures and with much more THz power than lasing from refilling inversion because the latter must overcome the effect of a much greater thermal population in the ground vibrational state that causes a greater threshold pump power.

Figure S6 shows the threshold power as a function of pressure for different direct transitions.  $J_L = 30$  has the lowest threshold across all pressures above 40 mTorr where optimal pressure appears as shown in Fig. S5. This corresponds to the observation

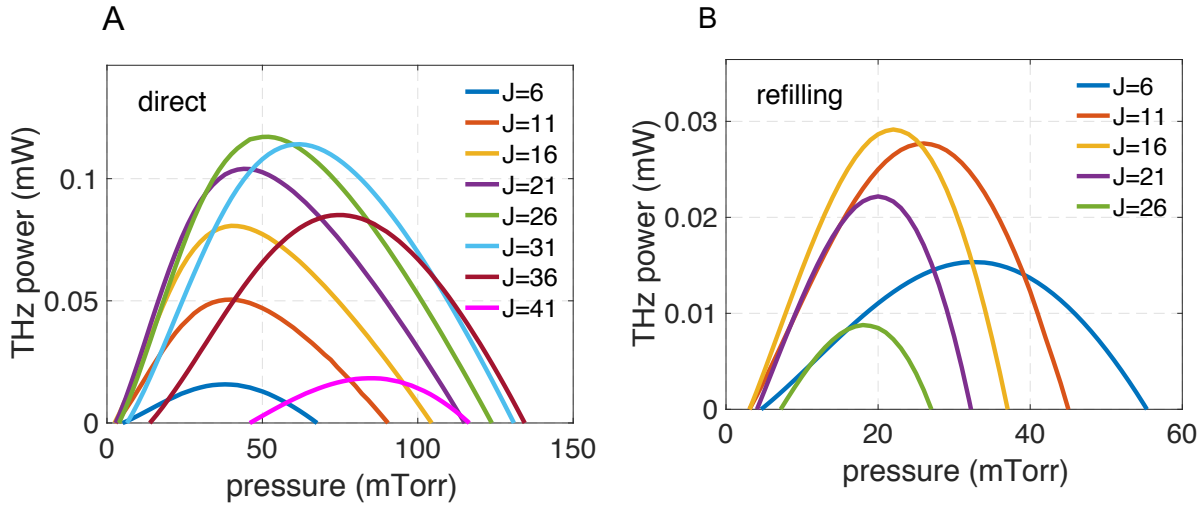


Figure S5. THz output power vs pressure with  $J_L = 6$  to  $J_L = 41$  for both direct and refilling lasing transitions.

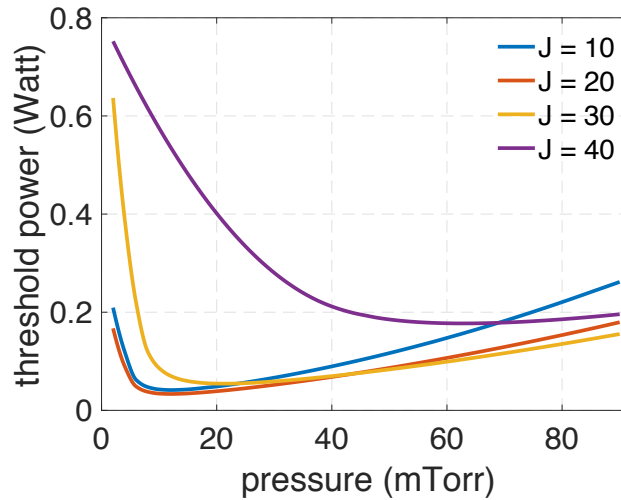


Figure S6. Pump threshold power as a function of pressure for  $J_L = 10, 20, 30, 40$ . The cavity loss is assumed to be  $0.3\text{m}^{-1}$  for all cases.

in the main text (Fig. 3B) that  $J_L = 28$  is predicted to produce the maximum power, even though the maximum population occurs at  $J_L = 15$ , because of the Manley–Rowe effect. A rotational state with  $J_L$  being either too large ( $J_L = 40$ ) or too small ( $J_L = 10$ ) has very limited population available to be pumped, therefore produces small gain to compensate the loss, leading to a high threshold. For  $J_L = 40$ , the threshold power increases with decreasing pressure below 60 mTorr. This is also an effect of a very limited population available to be pumped since the population fraction is only  $n_{J=40} = 0.54\%$ .

## V. ANALYTICAL DERIVATION OF THRESHOLD AND OUTPUT POWERS

In a simplified three-level model as shown in Fig. S7, population in the ground level 1 is pumped with rate  $R_{\text{pump}}$  into level 2, followed by dipole–dipole collisions between level 2 and level 3 and collisions with the cavity wall. THz lasing occurs between level 2 and 3. Similar three-level models can be found in previous work [32–34], but were not designed to describe the behavior at very low pressures in very small cavities. Note that the spontaneous emission rate is not used for obtaining the population inversion, because in these collision-dominant molecular gas lasers the spontaneous emission rate ( $1/t_{\text{sp}} \sim 10^{-5}\text{s}^{-1}$ ) is negligible compared with the dipole–dipole collision rate ( $k_{\text{DD}} \sim 10^5\text{s}^{-1}$ ). The spontaneous emission rate between levels 2 and 3 is used only for the gain calculation. In this section, analytical derivations of the population inversion, gain coefficient, pump threshold, and the THz output power in the low-pressure limit are presented.

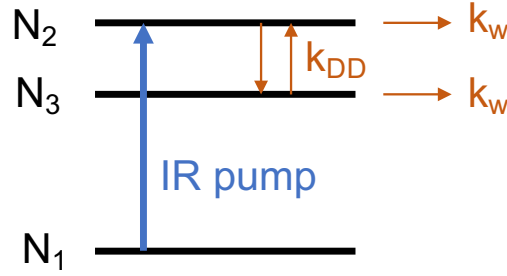


Figure S7. Schematics of a simplified three-level model for analytical derivations.

### A. Pump threshold

Assuming molecular relaxation is dominated by molecule–wall collisions with rate  $k_w$  and intermolecular dipole–dipole collisions with rate  $k_{DD}$ , the rate equations for  $N_2$  and  $N_3$  are

$$\begin{aligned}\frac{dN_2}{dt} &= R_{\text{pump}} - N_2(k_{DD} + k_w) + N_3k_{DD}, \\ \frac{dN_3}{dt} &= N_2k_{DD} - N_3(k_{DD} + k_w)\end{aligned}$$

At steady state,  $dN_2/dt = dN_3/dt = 0$ , and the population inversion is obtained as

$$\Delta N = N_2 - N_3 = \frac{R_{\text{pump}}}{2k_{DD} + k_w}. \quad (\text{S3})$$

The pump rate can be approximated as

$$R_{\text{pump}} = \frac{P_{\text{QCL}}(\alpha_{\text{IR}}L)}{h\nu_{\text{IR}}} \frac{1}{\pi R_{\text{cell}}^2 L} = \frac{\alpha_{\text{IR}}P_{\text{QCL}}}{\pi R_{\text{cell}}^2 h\nu_{\text{IR}}} \quad (\text{S4})$$

in which  $\alpha_{\text{IR}}$  is the infrared absorption coefficient of the gain medium, and  $R_{\text{cell}}$  and  $L$  are the cavity radius and length, respectively. The pump power absorbed by the gain medium is approximated as  $P_{\text{QCL}}(\alpha_{\text{IR}}L)$ .

The unsaturated gain coefficient is [35]

$$\gamma_0 = \sigma \Delta N = \left[ \frac{\lambda^2}{8\pi^2 \Delta\nu t_{\text{sp}}} \right] \Delta N$$

where  $\sigma$  is the cross section for the lasing transition, the spontaneous emission lifetime is  $t_{\text{sp}} = 3h\epsilon_0\lambda^3/16\pi^3\mu_{ij}^2$ , where  $\mu_{ij}^2 = |\langle i|\mu|j\rangle|^2$  is the dipole matrix element, and  $\Delta\nu$  is the half width at half maximum of the gain profile approximated in this low pressure regime as the Doppler broadening half width  $\Delta\nu \approx \Delta\nu_D \approx u/\lambda$ , where  $u$  is the average absolute molecular velocity. With temperature  $T$  and molecular mass  $m$ ,  $u = \sqrt{8k_B T/\pi m}$ . Then we obtain

$$\gamma_0 = \left( \frac{2}{3h^2\epsilon_0} \right) \left( \frac{\mu_{ij}^2}{uR_{\text{cell}}^2} \right) \left( \frac{\alpha_{\text{IR}}P_{\text{QCL}}}{\nu_{\text{IR}}} \right) \frac{1}{2k_{DD} + k_w}. \quad (\text{S5})$$

Threshold occurs when the unsaturated gain coefficient is equal to the cell loss,  $\gamma_0 = \alpha_{\text{cell}}$ , and the threshold power can be derived as [35]

$$P_{\text{th}} = \left( \frac{3h^2\epsilon_0\nu_{\text{IR}}}{2} \right) \left( \frac{uR_{\text{cell}}^2}{\mu_{ij}^2} \right) \left( \frac{\alpha_{\text{cell}}}{\alpha_{\text{IR}}} \right) (2k_{DD} + k_w) \quad (\text{S6})$$

At very low pressures in our very small cavity, where molecule–wall collisions dominate all other collisional processes,  $k_w \gg k_{DD}$ ,  $k_w \approx 2u/3R$ , and the pump threshold simplifies to

$$P_{\text{th}} = (h^2\epsilon_0\nu_{\text{IR}}) \left( \frac{u^2R_{\text{cell}}}{\mu_{ij}^2} \right) \left( \frac{\alpha_{\text{cell}}}{\alpha_{\text{IR}}} \right). \quad (\text{S7})$$

The above derivations are in SI units. The dipole moment needs to be converted by 1 Debye =  $3.33564 \times 10^{-30}$  C m. In Electrostatic CGS unit, Eq. (S7) is written as Eq. (2) in the main text by replacing  $\epsilon_0$  with  $1/4\pi$ .

## B. THz output power

Output power is obtained by equating the saturated gain to the cavity loss,

$$\gamma = \frac{\gamma_0}{1 + \Phi/\Phi_s} = \alpha_{\text{cell}} \quad (\text{S8})$$

in which  $\Phi$  is the photon flux density that is proportional to THz output power  $P_{\text{THz}}$ :

$$\begin{aligned} P_{\text{THz}} &= \frac{1}{2} h\nu_{\text{THz}} T (\pi R_{\text{cell}}^2) \Phi \\ &= \frac{1}{2} h\nu_{\text{THz}} T (\pi R_{\text{cell}}^2) \left( \frac{\gamma_0}{\alpha_{\text{cell}}} - 1 \right) \Phi_s \end{aligned} \quad (\text{S9})$$

where  $R_{\text{cell}}$  is the cavity radius,  $\Phi_s = k_s \Delta N / \gamma_0$  is the saturated photon flux density, and  $T$  is the power transmission coefficient of the front coupler. For wavelengths smaller than the pinhole diameter  $\lambda_{\text{THz}} < 2r_0$ ,  $T$  can be approximated as  $T \approx (\pi r_0 / \pi R_{\text{cell}})^2$ , but if the lasing wavelength is larger than  $2r_0$ ,  $T$  depends sensitively on the pinhole thickness. In the simple 3-level model,  $k_s$  can be derived as  $k_s = (2k_{\text{DD}} + k_w)/2$  following Ref. 35, and we obtain

$$\begin{aligned} P_{\text{THz}} &= \frac{1}{2} h\nu_{\text{THz}} (\pi r_0^2) \left( \frac{1}{\alpha_{\text{cell}}} - \frac{1}{\gamma_0} \right) \frac{\alpha_{\text{IR}} P_{\text{QCL}}}{2\pi R_{\text{cell}}^2 h\nu_{\text{IR}}} \\ &= \frac{1}{4} \frac{\nu_{\text{THz}}}{\nu_{\text{IR}}} \frac{r_0^2}{R_{\text{cell}}^2} \frac{\alpha_{\text{IR}}}{\alpha_{\text{cell}}} \left( 1 - \frac{\alpha_{\text{cell}}}{\gamma_0} \right) P_{\text{QCL}} \\ &= \frac{1}{4} \frac{\nu_{\text{THz}}}{\nu_{\text{IR}}} \frac{r_0^2}{R_{\text{cell}}^2} \frac{\alpha_{\text{IR}}}{\alpha_{\text{cell}}} (P_{\text{QCL}} - P_{\text{th}}). \end{aligned} \quad (\text{S10})$$

Relationship  $P_{\text{th}}/\alpha_{\text{cell}} = P_{\text{QCL}}/\gamma_0$  is used in the above derivation. The power efficiency equals the derivative of  $P_{\text{THz}}$  with respect to the pump power:

$$\eta = \frac{1}{4} \frac{\nu_{\text{THz}}}{\nu_{\text{IR}}} \frac{r_0^2}{R_{\text{cell}}^2} \frac{\alpha_{\text{IR}}}{\alpha_{\text{cell}}}. \quad (\text{S11})$$

Here are a few direct observations. The output power and power efficiency are proportional to the IR absorption coefficient  $\alpha_{\text{IR}}$ . Since  $\alpha_{\text{IR}}$  is proportional to the molecular pressure  $p$  and the population fraction of rotational level  $J_L$ , we have  $P_{\text{THz}}, \eta \propto \alpha_{\text{IR}} \propto p n_{J_L}$ . The output power and power efficiency are also proportional to the THz frequency, i.e.,  $P_{\text{THz}}, \eta \propto \nu_{\text{THz}}/\nu_{\text{IR}}$ , which is the Manley–Rowe effect.

In this derivation, it was assumed that the linewidth of the QCL was much narrower than the Doppler width of the pumped infrared transition, and indeed this is the case. Our experimental QCL is specified by the manufacturer to have a linewidth in the range of 1-10 MHz, also confirmed by other measurements [24], compared to the 50-150 MHz linewidth of typical molecular infrared transitions. Our analysis finds excellent agreement with the experimental results for a QCL linewidth of 2 MHz. If the QCL linewidth were larger, the simple model derived here could reflect this fact by using an averaged  $\alpha_{\text{IR}}$ , obtained by a convolution of the QCL and Doppler lineshapes, rather than using the above approximation of  $\alpha_{\text{IR}}$  at its center frequency. Regarding the linewidth of the QPML laser transition, these lasers are perhaps more appropriately called “masers” [36] because their cavity linewidths ( $\approx 10$ -100 MHz) are larger than the molecular gain profile ( $\approx 1$  MHz).

## VI. USING AMMONIA (NH<sub>3</sub>) AS A QPML GAIN MEDIUM

The oblate molecule ammonia (NH<sub>3</sub>) combines many of the most attractive attributes for QPML operation: a low lying vibrational mode with a strong IR absorption coefficient and a large permanent dipole moment. Consequently, the simple model predicts that it will have low threshold and high power efficiency, attributes that should produce the strongest lines of the nine molecules considered here. Note that unlike the ground state inversion, which occurs at a relatively low frequency of 24 GHz, the inversion splitting in  $v_2 = 1$  vibrational mode near 950 cm<sup>-1</sup> is much larger, approximately 1 THz. Figure S8 plots the predicted laser lines for the strongest pure inversion and rotation-inversion transitions in NH<sub>3</sub>, spanning transitions up to  $J = 9$  excited by Q-branch transitions between 930 - 936 cm<sup>-1</sup> and 962 - 968 cm<sup>-1</sup>. The strongest laser lines are those for which  $J=K$  or  $K-1$ . Operation on several of pure-inversion lines near 1 THz has recently been experimentally shown [14] but the limited tuning range of pure inversion transitions minimizes the effectiveness of the Manley-Rowe factor.

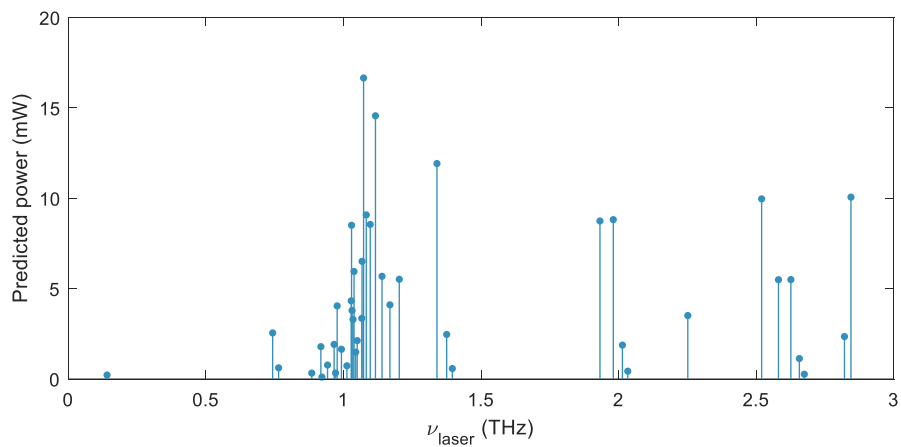


Figure S8. Plot showing the emission frequency and power predicted by the simple model for 20 mTorr of ammonia in a compact cylindrical cavity pumped by a 0.25 W QCL for emission frequency between 0 and 3 THz.

## References and Notes

1. T. Nagatsuma, G. Ducournau, C. C. Renaud, Advances in terahertz communications accelerated by photonics. *Nat. Photonics* **10**, 371–379 (2016). [doi:10.1038/nphoton.2016.65](https://doi.org/10.1038/nphoton.2016.65)
2. R. A. Lewis, A review of terahertz sources. *J. Phys. D Appl. Phys.* **47**, 374001 (2014). [doi:10.1088/0022-3727/47/37/374001](https://doi.org/10.1088/0022-3727/47/37/374001)
3. A. Maestrini, J. S. Ward, J. J. Gill, C. Lee, B. Thomas, R. H. Lin, G. Chattopadhyay, I. Mehdi, A frequency-multiplied source with more than 1 mW of power across the 840–900-GHz band. *IEEE Trans. Microw. Theory Tech.* **58**, 1925–1932 (2010). [doi:10.1109/TMTT.2010.2050171](https://doi.org/10.1109/TMTT.2010.2050171)
4. J. H. Booske, R. J. Dobbs, C. D. Joye, C. L. Kory, G. R. Neil, G.-S. Park, J. Park, R. J. Temkin, Vacuum electronic high power terahertz sources. *IEEE Trans. Terahertz Sci. Technol.* **1**, 54–75 (2011). [doi:10.1109/TTHZ.2011.2151610](https://doi.org/10.1109/TTHZ.2011.2151610)
5. Y. Shen, P. Upadhyaya, E. Linfield, H. Beere, A. Davies, Ultrabroadband terahertz radiation from low-temperature-grown GaAs photoconductive emitters. *Appl. Phys. Lett.* **83**, 3117–3119 (2003). [doi:10.1063/1.1619223](https://doi.org/10.1063/1.1619223)
6. K. McIntosh, E. R. Brown, K. B. Nichols, O. B. McMahon, W. F. DiNatale, T. M. Lyszczarz, Terahertz photomixing with diode lasers in low-temperature-grown GaAs. *Appl. Phys. Lett.* **67**, 3844–3846 (1995). [doi:10.1063/1.115292](https://doi.org/10.1063/1.115292)
7. K. Evenson, D. Jennings, F. Petersen, Tunable far-infrared spectroscopy. *Appl. Phys. Lett.* **44**, 576–578 (1984). [doi:10.1063/1.94845](https://doi.org/10.1063/1.94845)
8. M. Inguscio, P. D. Natale, L. Veseth, *Comments At. Mol. Phys.* **30**, 3 (1994).
9. R. Köhler, A. Tredicucci, F. Beltram, H. E. Beere, E. H. Linfield, A. G. Davies, D. A. Ritchie, R. C. Iotti, F. Rossi, Terahertz semiconductor-heterostructure laser. *Nature* **417**, 156–159 (2002). [doi:10.1038/417156a](https://doi.org/10.1038/417156a) [Medline](#)
10. L. Bosco, M. Franckić, G. Scalari, M. Beck, A. Wacker, J. Faist, Thermoelectrically cooled THz quantum cascade laser operating up to 210 K. *Appl. Phys. Lett.* **115**, 010601 (2019). [doi:10.1063/1.5110305](https://doi.org/10.1063/1.5110305)
11. C. A. Curwen, J. L. Reno, B. S. Williams, Broadband continuous single-mode tuning of a short-cavity quantum-cascade VECSEL. *Nat. Photonics* 10.1038/s41566-019-0518-z (2019). [doi:10.1038/s41566-019-0518-z](https://doi.org/10.1038/s41566-019-0518-z)
12. T. Chang, T. Bridges, E. Burkhardt, Submillimeter laser action in optically pumped methyl fluoride, methyl alcohol, and vinyl chloride gases. *Appl. Phys. Lett.* **17**, 249–251 (1970). [doi:10.1063/1.1653386](https://doi.org/10.1063/1.1653386)
13. J. Faist, F. Capasso, D. L. Sivco, C. Sirtori, A. L. Hutchinson, A. Y. Cho, Quantum cascade laser. *Science* **264**, 553–556 (1994). [doi:10.1126/science.264.5158.553](https://doi.org/10.1126/science.264.5158.553) [Medline](#)
14. A. Pagies, G. Ducournau, J.-F. Lampin, Low-threshold terahertz molecular laser optically pumped by a quantum cascade laser. *APL Photonics* **1**, 031302 (2016). [doi:10.1063/1.4945355](https://doi.org/10.1063/1.4945355)

15. I. Gordon, L. S. Rothman, C. Hill, R. V. Kochanov, Y. Tan, P. F. Bernath, M. Birk, V. Boudon, A. Campargue, K. V. Chance, B. J. Drouin, J.-M. Flaud, R. R. Gamache, J. T. Hodges, D. Jacquemart, V. I. Perevalov, A. Perrin, K. P. Shine, M.-A. H. Smith, J. Tennyson, G. C. Toon, H. Tran, V. G. Tyuterev, A. Barbe, A. G. Császár, V. M. Devi, T. Furtenbacher, J. J. Harrison, J.-M. Hartmann, A. Jolly, T. J. Johnson, T. Karman, I. Kleiner, A. A. Kyuberis, J. Loos, O. M. Lyulin, S. T. Massie, S. N. Mikhailenko, N. Moazzen-Ahmadi, H. S. P. Müller, O. V. Naumenko, A. V. Nikitin, O. L. Polyansky, M. Rey, M. Rotger, S. W. Sharpe, K. Sung, E. Starikova, S. A. Tashkun, J. V. Auwera, G. Wagner, J. Wilzewski, P. Wcisło, S. Yu, E. J. Zak, The HITRAN2016 molecular spectroscopic database. *J. Quant. Spectrosc. Radiat. Transf.* **203**, 3–69 (2017). [doi:10.1016/j.jqsrt.2017.06.038](https://doi.org/10.1016/j.jqsrt.2017.06.038)
16. JPL Molecular Spectroscopy Database (2017); <https://spec.jpl.nasa.gov/>.
17. Splatalogue Database for Astronomical Spectroscopy (2007); <http://www.cv.nrao.edu/php/splat/>.
18. C. Townes, A. L. Schawlow, *Microwave Spectroscopy* (Dover Publications, 1995).
19. W. Gordy, R. L. Cook, *Microwave Molecular Spectroscopy* (Wiley-Interscience, 1984).
20. H. O. Everitt, D. D. Skatrud, F. C. DeLucia, Dynamics and tunability of a small optically pumped cw far-infrared laser. *Appl. Phys. Lett.* **49**, 995–997 (1986). [doi:10.1063/1.97469](https://doi.org/10.1063/1.97469)
21. R. McCormick, H. Everitt, F. DeLucia, D. Skatrud, Collisional energy transfer in optically pumped far-infrared lasers. *IEEE J. Quantum Electron.* **23**, 2069–2077 (1987). [doi:10.1109/JQE.1987.1073302](https://doi.org/10.1109/JQE.1987.1073302)
22. S.-L. Chua, C. A. Caccamise, D. J. Phillips, J. D. Joannopoulos, M. Soljačić, H. O. Everitt, J. Bravo-Abad, Spatio-temporal theory of lasing action in optically-pumped rotationally excited molecular gases. *Opt. Express* **19**, 7513–7529 (2011). [doi:10.1364/OE.19.007513](https://doi.org/10.1364/OE.19.007513) [Medline](#)
23. F. Wang, J. Lee, D. J. Phillips, S. G. Holliday, S.-L. Chua, J. Bravo-Abad, J. D. Joannopoulos, M. Soljačić, S. G. Johnson, H. O. Everitt, A high-efficiency regime for gas-phase terahertz lasers. *Proc. Natl. Acad. Sci. U.S.A.* **115**, 6614–6619 (2018). [doi:10.1073/pnas.1803261115](https://doi.org/10.1073/pnas.1803261115) [Medline](#)
24. K. Knabe, P. A. Williams, F. R. Giorgetta, C. M. Armacost, S. Crivello, M. B. Radunsky, N. R. Newbury, Frequency characterization of a swept- and fixed-wavelength external-cavity quantum cascade laser by use of a frequency comb. *Opt. Express* **20**, 12432–12442 (2012). [doi:10.1364/OE.20.012432](https://doi.org/10.1364/OE.20.012432) [Medline](#)
25. See supplementary materials.
26. R. Bansal, *Fundamentals of Engineering Electromagnetics* (CRC Press, 2006).
27. J. Manley, H. Rowe, Some general properties of nonlinear elements-Part I. General energy relations. *Proceedings of the IRE* **44**, 904–913 (1956). [doi:10.1109/JRPROC.1956.275145](https://doi.org/10.1109/JRPROC.1956.275145)
28. H. O. Everitt, F. C. De Lucia, Rotational energy transfer in small polyatomic molecules. *Adv. At. Mol. Opt. Phys.* **35**, 331–400 (1995). [doi:10.1016/S1049-250X\(08\)60166-4](https://doi.org/10.1016/S1049-250X(08)60166-4)

29. R. M. Williams, J. F. Kelly, J. S. Hartman, S. W. Sharpe, M. S. Taubman, J. L. Hall, F. Capasso, C. Gmachl, D. L. Sivco, J. N. Baillargeon, A. Y. Cho, Kilohertz linewidth from frequency-stabilized mid-infrared quantum cascade lasers. *Opt. Lett.* **24**, 1844–1846 (1999). [doi:10.1364/OL.24.001844](https://doi.org/10.1364/OL.24.001844) [Medline](#)
30. R. L. Crownover, H. O. Everitt, F. C. De Lucia, D. D. Skatrud, Frequency stability and reproducibility of optically pumped far-infrared lasers. *Appl. Phys. Lett.* **57**, 2882–2884 (1990). [doi:10.1063/1.103765](https://doi.org/10.1063/1.103765)
31. P. R. Amestoy, I. S. Duff, J.-Y. L'Excellent, Multifrontal parallel distributed symmetric and unsymmetric solvers. *Comput. Methods Appl. Mech. Eng.* **184**, 501–520 (2000). [doi:10.1016/S0045-7825\(99\)00242-X](https://doi.org/10.1016/S0045-7825(99)00242-X)
32. R. J. Temkin, D. R. Cohn, Rate equations for an optically-pumped, far infrared laser. *Optics Communications* **16**, 213–217 (1976). [doi:10.1016/0030-4018\(76\)90220-0](https://doi.org/10.1016/0030-4018(76)90220-0)
33. R. Panock, R. Temkin, Interaction of two laser fields with a three-level molecular system. *IEEE J. Quantum Electron.* **13**, 425–434 (1977). [doi:10.1109/JQE.1977.1069354](https://doi.org/10.1109/JQE.1977.1069354)
34. D. A. McQuarrie, J. D. Simon, *Physical Chemistry: A Molecular Approach* (University Science Books, 1997).
35. B. E. A. Saleh, M. C. Teich, *Fundamentals of Photonics*, vol. 22 of *Wiley Series in Pure and Applied Optics* (Wiley, 1991).
36. A. L. Schawlow, C. H. Townes, Infrared and optical masers. *Phys. Rev.* **112**, 1940–1949 (1958). [doi:10.1103/PhysRev.112.1940](https://doi.org/10.1103/PhysRev.112.1940)